Journal of Materials Processing Tech. 288 (2021) 116913

Contents lists available at ScienceDirect

Journal of Materials Processing Tech.

journal homepage: www.elsevier.com/locate/jmatprotec

Geometrical effect on macrosegregation formation during unidirectional solidification of Al–Si alloy

Haijie Zhang [a], Menghuai Wu [a,*], Surendra N. Tewari [b], Andreas Ludwig [a], Abdellah Kharicha [a]

[a] Chair for Simulation and Modelling of Metallurgy Processes, Department of Metallurgy, University of Leoben, A-8700 Leoben, Austria
[b] Chemical and Biomedical Engineering Department, Cleveland State University, Cleveland, OH, 44115, United States

ARTICLE INFO

Associate Editor: A Luo

Keywords:
Geometrical effect
Macrosegregation
Unidirectional solidification
Solidification shrinkage
Stray crystals

ABSTRACT

In the production of single-crystal turbine blades for use in aircraft engines with unidirectional solidification techniques, it is confirmed that the casting geometry had great influence on the formation of macrosegregation or spurious/stray crystals. In this study, a two-phase solidification model is used to investigate the geometrical effect on the unidirectional solidification of Al–7.0 wt.% Si alloy. The study is based on the experiment of Ghods et al. (2016a), in which the diameter of the sample is changed between ϕ9.5 and ϕ3.2 mm along the solidification direction to highlight the geometrical effect. The first part of the investigation is to verify the numerical model by 'reproducing' the experimentally obtained macrosegregation and phase distribution in an as-cast sample. The second part is to explore the macrosegregation mechanism. It is found that the main geometrical effect is the modification of the bulk and the interdendritic melt flow during solidification. Different flow patterns are found in different locations, e.g. below or above the cross-section contraction; however, details of the macrosegregation formation can be explained by a scalar product of two vectors, i.e. the flow velocity and the concentration gradient of the melt. Based on the positive/negative value of the scalar product, i.e. the flow direction in comparison with the direction of the concentration gradient, it is possible to determine where a negative/positive segregation will occur. The above scalar product is also found valid for analysing the possible formation of spurious/stray crystals, and it is numerically demonstrated that the cross-section expansion in casting geometry leads to high risk of spurious/stray crystals.

1. Introduction

The casting geometry is an important factor influencing the melt flow pattern during solidification, and an inappropriate geometry design may intensify macrosegregation or cause formation of other defects. Turbine blades, which are key components in aircraft engines, are produced as single crystals by a unidirectional solidification technique. However, several geometrical features of the turbine blade casting, e.g. abrupt change in the casting section, can lead to onset of freckles ('channel segregates') or formation of spurious/stray crystals, which severely deteriorate the creep-rupture life of single-crystal blades. Freckle appears as solute-enriched phases and long chain of equiaxed grains in the direction roughly parallel to the gravity. It is generally believed that the formation of freckles is caused by the thermo-solutal convection. Recent investigation by Ma and Bührig-Polaczek (2014) confirmed that the casting geometry significantly affected the onset of freckles during the unidirectional solidification.

Flemings et al. (1968) carried out a unidirectional solidification experiment with a casting sample of cross-section contraction, and they found a positive macrosegregation before the cross-section contraction, and a strong negative macrosegregation after the cross-section contraction. Ma et al. (2012) performed experiments to investigate the geometrical effect on the freckle formation in superalloy components. The sudden contraction of the cross-section revealed a promoting eff ;ect on the freckle onset. With cross section expansion, the freckles did not occur immediately after the cross-section expansion, but the freckles occurred after an incubation distance. The above experiments studies were extended by Hong et al. (2015) with numerical modelling, and improved knowledge about the freckle formation was obtained by considering the geometrical effect on the local heat transfer and flow pattern. In the Hong's work macrosegregation was not directly modelled.

Ghods et al. (2016a) performed a unidirectional solidification experiment with both cross-section contraction and expansion between

* Corresponding author.
E-mail address: menghuai.wu@unileoben.ac.at (M. Wu).

https://doi.org/10.1016/j.jmatprotec.2020.116913
Received 19 May 2020; Received in revised form 10 August 2020; Accepted 21 September 2020
Available online 24 September 2020
0924-0136/

ϕ9.5 and ϕ3.2 mm in one cylindrical casting sample (Al–7 wt.% Si). In the meantime the authors Ghods et al. (2016b) did numerical analysis of the experiment. As a 2D planar simulation, instead of 2D axi-symmetrical or 3D simulation, was made, the modelling results could only be used to explain the experimental phenomena qualitatively. Although no notable freckle and spurious crystals were observed in the small casting sample, a few misoriented dendrite fragments near the sample surface were detected by Ghods et al. (2018). This unidirectional solidification experiment provides an excellent benchmark for further development of the numerical models.

A series of multiphase solidification models were developed. Wu et al. (2019) did a comprehensive review recently. Those models have been evaluated with some benchmark castings and also applied to predict the macrosegregation in large steel ingots. The current study uses a multiphase volume-average-based solidification model to simulate the Ghods' experiment. The main goal is to investigate the macrosegregation mechanism induced by the geometry as well as the potential impact of the casting geometry on the formation of spurious grains. A further goal is to verify the numerical model.

2. Model description and simulation settings

As-solidified casting samples are experimentally observed to be dominant in columnar structures. Therefore, a two-phase solidification model was considered here. Wu et al. (2016) have described details of this model. The main features/assumptions are outlined below.

(1) The two phases refer to solid columnar and liquid melt.
(2) The columnar morphology is simplified as cylinders growing unidirectionally along the temperature gradient. The columnar tip front is traced according to the LGK model reported by Lipton et al. (1984).
(3) The arm spacing of the primary and secondary dendrites, λ_1 and λ_2, taken from the as-solidified structure measured by Ghods et al. (2016a), are assumed to be constant during solidification.
(4) The average liquid and solid concentrations are calculated. The solid-liquid interface is presumed to be thermodynamic equilibrium.

Table 1
Summary of the material properties and other parameters (Ghods et al., 2016a; Zhang et al., 2020).

Properties/parameters	Symbol	Units	Values
Thermophysical			
Specific heat of the alloy	c_p^ℓ c_p^s	$J\,kg^{-1}\,K^{-1}$	1170.0
Specific heat of the mould	c_m	$J\,kg^{-1}\,K^{-1}$	1570.0
Latent heat	Δh_f	$J\,kg^{-1}$	4.0×10^5
Solid diffusion coefficient	D_c	$m^2{\cdot}s^{-1}$	1.0×10^{-12}
Liquid diffusion coefficient	D_ℓ	$m^2{\cdot}s^{-1}$	6.45×10^{-9}
Liquid thermal conductivity	k_ℓ	$W\,m^{-1}\,K^{-1}$	76.7
Solid thermal conductivity	k_s	$W\,m^{-1}\,K^{-1}$	185.0
Mould thermal conductivity	k_m	$W\,m^{-1}\,K^{-1}$	65.0
Liquid thermal expansion coefficient	β_T	K^{-1}	-1.85×10^{-4}
Liquid solutal expansion coefficient	β_c	$wt.\%^{-1}$	1.31×10^{-3}
Liquid density	ρ_ℓ	$kg\,m^{-3}$	2408.0
Solid density	ρ_s	$kg\,m^{-3}$	2545.0
Mould density	ρ_m	$kg\,m^{-3}$	2100.0
Viscosity	μ_ℓ	$kg\,m^{-1}{\cdot}s^{-1}$	1.16×10^{-3}
Thermodynamic			
Eutectic composition	c_{eu}	wt.%	12.6
Eutectic temperature	T_{eut}	K	850.15
Liquidus slope	m	$K\,(wt.\%)^{-1}$	−7.619
Equilibrium partition coefficient	k	–	0.131
Primary dendritic arm spacing	λ_1	μm	300.0
Secondary arm spacing	λ_2	μm	50.0
Gibbs Thomson coefficient	Γ	m K	2.41×10^{-7}
Melting point of the solvent	T_f	K	946.15
Others			
Initial concentration	c_0	wt.% Si	7.0
Initial temperature	T_0	K	1200.0
Cooling rate of the top and the bottom	R	K/s	0.148
Temperature gradient	$\vec{G}$	K/m	5100.0
Withdrawal velocity	v	μm/s	29.1

(5) A shrinkage-induced flow is considered. According to Magnusson and Arnberg (2001), the density of the as-solidified eutectic phase

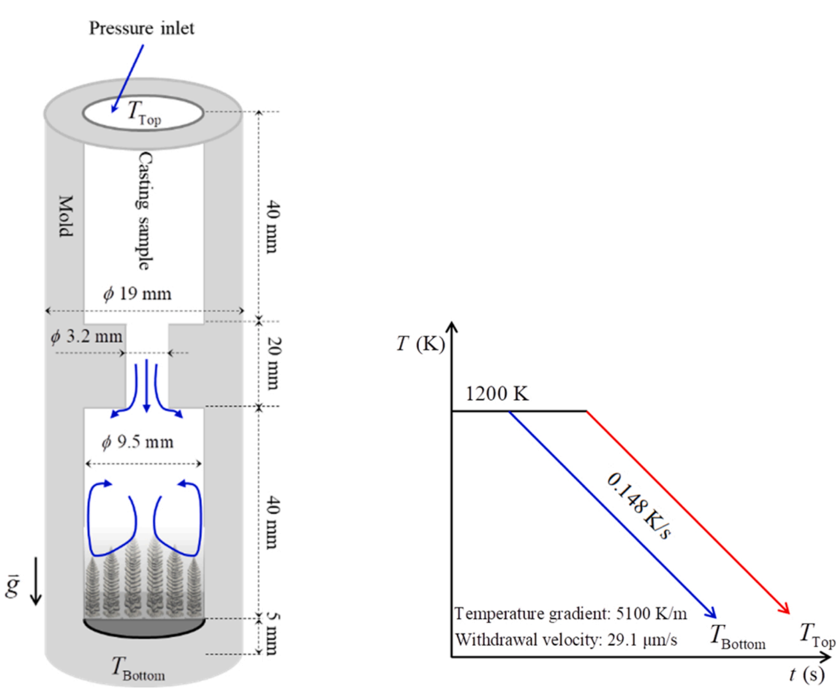

Fig. 1. Geometry configuration and boundary conditions.

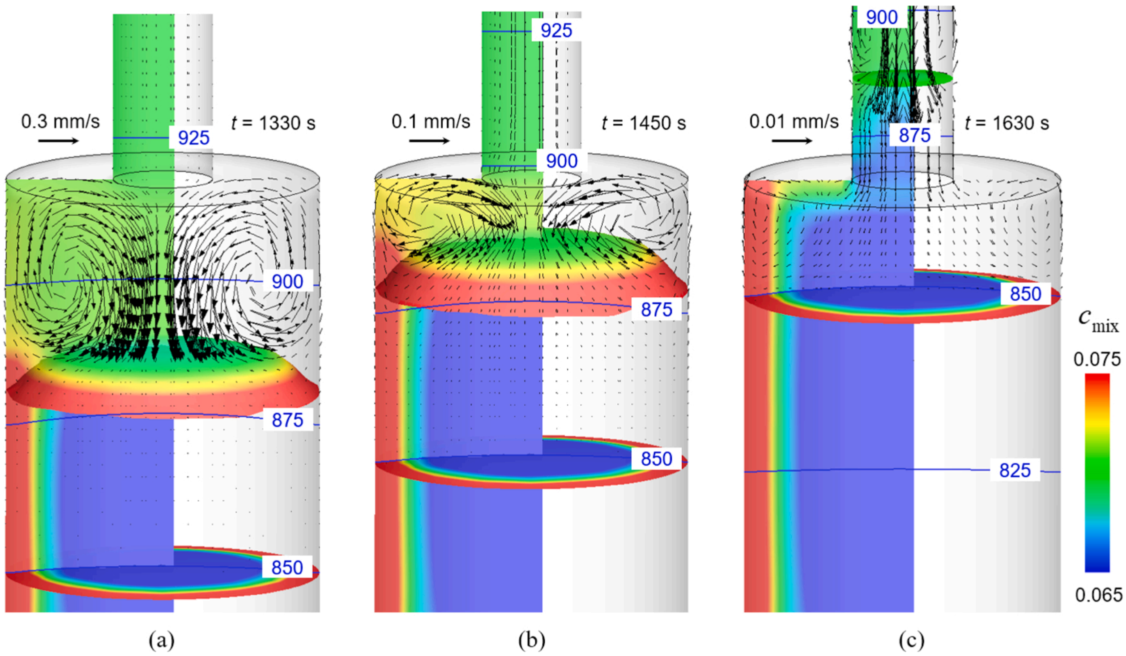

Fig. 2. Solidification sequence when the columnar tip front (iso-surface of $f_\ell = 0.95$) approaches and passes the position of the cross-section contraction: (a) $t = 1330$s; (b) $t = 1450$s; (c) $t = 1630$s. Vectors on the vertical section of the sample indicate the liquid velocity, overlaid by isotherms (solid lines). Two iso-surfaces depict the mushy zone: top one for $f_\ell = 0.95$, bottom one for $T_{eut} = 850$ K. The colour in all the section/iso-surfaces denotes c_{mix}.

is similar to the density of the primary dendrites. The thermo-solutal convection is modelled using the Boussinesq approach.

(6) As the secondary dendrite arm space changes during solidification due to the fact of coarsening, permeability of the mushy zone is treated as a function of the liquid volume fraction and primary dendrite arm space.

(7) The mixture concentration is calculated by $c_{mix} = (f_\ell \cdot \rho_\ell \cdot c_\ell + f_c \cdot \rho_c \cdot c_c)/(f_\ell \cdot \rho_\ell + f_c \cdot \rho_c)$, and macrosegregation is characterized by the segregation index, $c^{index} = (c_{mix} - c_0) \times 100/c_0$, in which c_ℓ and c_c are the concentrations of the liquid and columnar, respectively.

Ghods et al. (2016a) published the cooling conditions of the casting sample (Al–7.0 wt.% Si). A graphite crucible (mould) of 30 cm in length was used. The first part of the crucible cavity (casting sample) was 130 mm in length and ϕ9.5 mm in diameter; in the second part, the sample section was reduced to the diameter of ϕ3.2 mm for a length of 50 mm. In the third part, the sample section was increased to ϕ9.5 mm for a length of 120 mm. In the simulation, however, only 105 mm of the crucible is simulated, including the two large section zones and one small section zone, as displayed in Fig. 1. The reason why such a length is chosen will be discussed later. The calculation is initialized with a constant temperature (T_0) in the alloy and the crucible and a homogeneous solute distribution (c_0) in the alloy. On the top and bottom, a Dirichlet boundary condition (decreasing temperature: T_{Top} and T_{Bottom}), which corresponds to the experimentally imposed temperature gradient ($\vec{G}$) and withdrawal speed (v), is applied. The temperature boundary condition on the outer wall of the crucible is a spatial interpolation of T_{Top} and T_{Bottom}. A pressure inlet is applied on the top surface of the sample, and a hot melt is allowed to feed the solidification shrinkage. At the mould–alloy interface, a non-slip boundary condition is used for the melt flow. All the material properties of the alloy and the crucible can be found in Table 1.

The model is implemented in ANSYS FLUENT version 17.1. A control-volume based Eulerian–Eulerian multiphase solver is used. The maximum volume element (mesh) sizes are 3.5×10^{-4} m (3D) and 1.0×10^{-4} m (2D), respectively. The time step is set as 5×10^{-4} s. A maximum of 30 iterations per time step are conducted to ensure normalized residuals of the concentration and flow quantities, continuity below 10^{-4}, and enthalpy quantities below 10^{-7}. One 3D and 2D simulations requires 6 and 2 weeks, respectively, on a high-performance cluster (2.6 GHz, 28 cores).

3. Simulation results

3.1. Solidification process

The solidification sequence when the columnar tip front approaches and passes the position of the cross-section contraction is displayed in Fig. 2. The mushy zone is represented and confined by two iso-surfaces: top one for $f_\ell = 0.95$, and bottom one for T_{eut}. At $t = 1330$s (Fig. 2(a)), the solidification front is still far from the position of the cross-section contraction. The thermal conductivity of the solid phase is higher than those of the graphite mould and liquid phase ($k_s \approx 2.5k_\ell$ or$2.8k_m$), and this causes a radial heat transfer from the graphite mould to the casting sample towards the solidification front. In the sample centre, a so-called 'steepling convection' is developed, and the solidification front is bulged. The bulk melt streams downwards to the sample centre against the solidification front, penetrating into the mushy zone, subsequently flows gradually along the curved profile of the mushy zone towards the periphery of the sample, and finally rises upwards at the sample surface. The solute-enriched interdendritic melt is gradually transported from the sample centre to the periphery. This type of solute transport causes a negative macrosegregation at the casting centre and a positive macrosegregation at the outer periphery. Concurrently, it causes a speed-up of the solidification in the sample centre and a slow-down of the solidification in the outer periphery. This suggests that the steepling convection accelerates itself, causing the solidification front to become more bulged. The liquid velocity reaches as high as 406 μm/s, which is mainly driven by the thermo-solutal buoyancy. Zhang et al. (2018) studied the flow pattern and solute macrosegregation under pure shrinkage-induced feeding flow condition. They found that the pure shrinkage-induced feeding flow in this section was much slower (1.3 μm/s)

At 1450s, when the solidification front is approaching the position of

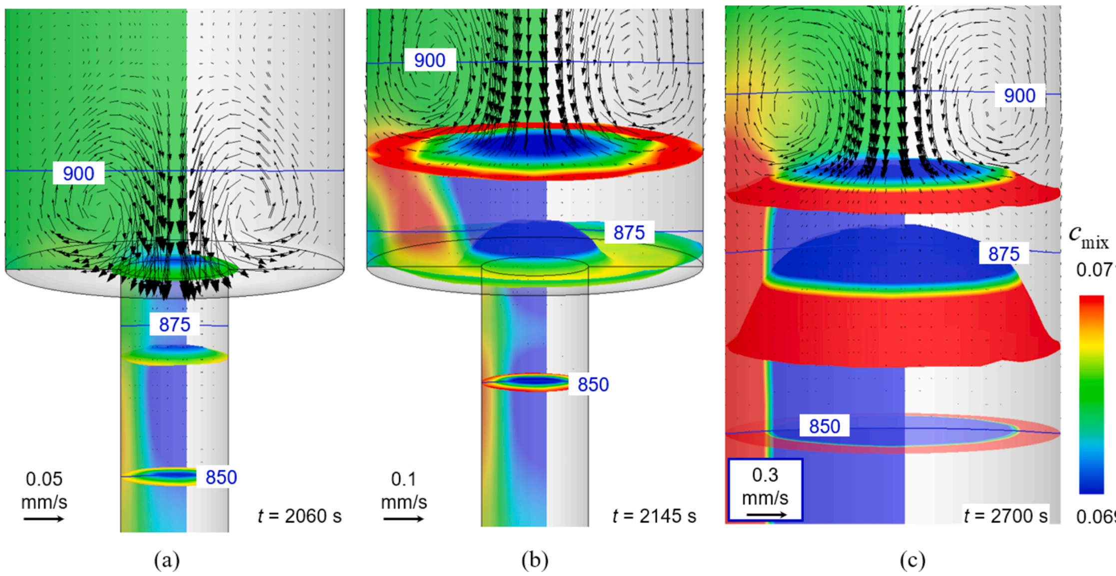

Fig. 3. Solidification sequence when columnar tip front (iso-surface of $f_\ell = 0.95$) reaches and passes the position of the cross-section expansion: (a) $t = 2060$s; (b) $t = 2145$s; (c) $t = 2700$s. Vectors on the vertical section of the sample indicate the liquid velocity, overlaid by the isotherms (solid lines). The two iso-surfaces display the mushy zone: top one for $f_\ell = 0.95$, bottom one for $T_{eut} = 850$ K. An additional iso-surface ($f_\ell = 0.7$) is drawn in the mushy zone. The colour in all the section/iso-surfaces denotes c_{mix}.

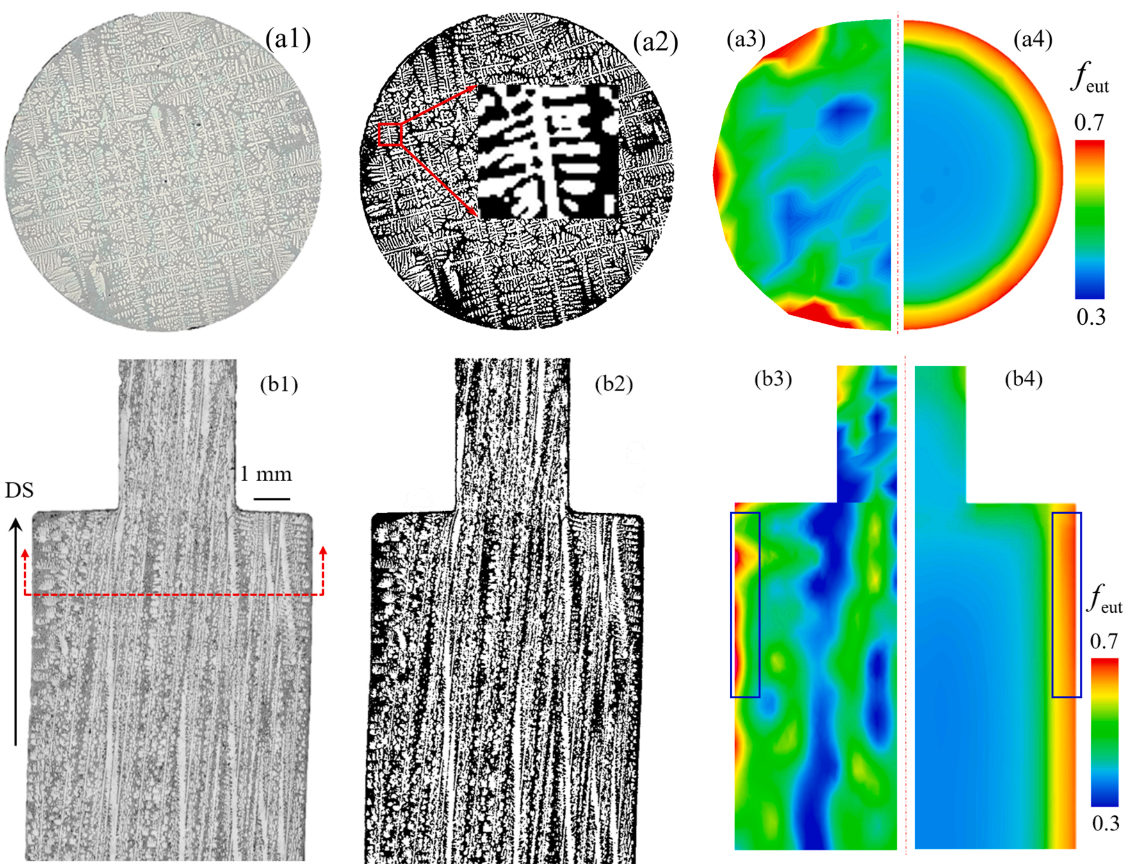

Fig. 4. Experiment–simulation comparison of the phase distribution. The first row displays the transverse section of the sample, and the second row depicts the vertical section of the sample. (a1) and (b1) Metallography with bright region denoting the primary dendrites and dark region denoting the eutectic phase. (a2) and (b2) Binary threshold images: primary dendrite is in white colour and eutectic phase is in black. (a3) and (b3) Distribution of the volume fraction of the eutectics (f_{eut}) from the experimental results. (a4) and (b4) Simulated distribution of f_{eut}. The position of the transverse section in the first row is marked by a dashed line in (b1). Figs. (a1) and (b1) are reproduced from (Ghods et al., 2016a, 2016b) with permission of Elsevier.

the cross-section contraction (Fig. 2**(b)**), the space for the bulk flow is largely limited to the volume between the columnar tip front and the 'shoulder' of the sample. Owing to this space limitation, the maximum liquid velocity reduces to 93 μm/s. The solidification shrinkage-induced feeding flow in the small-section zone becomes more significant. Although the shrinkage-induced flow acts in the same direction as the thermo-solutal convection in the casting centre, it is not sufficient to compensate the effect of the space limitation. From c_{mix}, the bulk liquid between the columnar tip front and the sample shoulder enriched with solute can be seen.

Fig. 2**(c)** depicts the simulation result at 1630s when the solidification tip front passes the position of the cross-section contraction. Above the solidification front, the steepling convection also develops in a small section, but the bulk liquid velocity (~17 μm/s) is weaker than that presented in Fig. 2**(a)**. In the mush, the interdendritic melt flows downward to compensate the volume shrinkage. In the large cross-section zone, the steepling convection can still be observed in the mushy zone near the sample shoulder surface, but with a low intensity (~5 μm/s). This interdendritic flow, despite its low intensity, strengthens the positive macrosegregation below the sample shoulders significantly. A solute-depleted region covering the whole cross-section of the sample is observed exactly above the cross-section contraction.

Fig. 3 displays the solidification sequence near the cross-section expansion. As the solidification front reaches the position of the cross-section expansion (Fig. 3**(a)**), the bulk flow is still quite weak (50 μm/s); only a weak negative macrosegregation forms at the sample centre. After the solidification front passes the cross-section expansion (Fig. 3 **(b)**), a flow pattern similar to that in Fig. 2**(a)** develops. The iso-surface of $f_\ell = 0.7$ appears like a growing mushroom: a small cap develops from the contraction zone, which subsequently grows and extends sideways along the platform of the expansion region. At 2700s (Fig. 3**(c)**) the bulk flow becomes stronger (243 μm/s). The melt, as enriched with solute, accumulates near the sample surface, and suppresses the solidification locally. The solidification front becomes further bulged, and the aforementioned steepling convection continues again.

3.2. Model validation

3.2.1. Phase distribution

The numerically calculated eutectic phase distribution (f_{eut}) is compared with metallography performed on an as-cast sample, as displayed in Fig. 4. The Al–7.0 wt.% Si alloy mainly solidifies as primary aluminium dendrites with embedded eutectics. Fig. 4**(a1)** and **(b1)** present the original metallographic images. They were first converted to 8-bits, and subsequently the eutectic component was depicted in black and the primary aluminium dendrites in white (Fig. 4**(a2)** and **(b2)**) by adjusting the contrast 'threshold' in the ImageJ software. These black and white images were cut into small rectangular blocks of sizes 0.6 × 0.6 mm using MATLAB software. The area fraction of the black area in each block (e.g. a zoom-in view in Fig. 4**(a2)**) was counted, and the counting results are plotted as contours in Fig. 4**(a3)** and **(b3)**. The eutectic phase distributes non-uniformly. Significant eutectic phase accumulates at the sample surface. The simulation results are displayed in Fig. 4**(a4)** and **(b4)**. Consistent with the experimental results in Fig. 4 **(a3)** and **(b3)**, the eutectic phase accumulates near the sample surface, particularly before the cross-section contraction (the blue rectangles in Fig. 4**(b3)** and **(b4)**), whereas that in the sample centre is depleted. As reported by Ghods et al. (2016a), owing to the dendrite 'clustering' during the solidification, the microstructures in the different vertical sections are different. A better approach to validate the simulation results is to average the experimentally observed eutectic distribution in the different vertical sections, so that the dark blue region in Fig. 4**(b3)** disappears.

3.2.2. Macrosegregation

The experiment–simulation comparison of macrosegregation is presented in Fig. 5. The macrosegregation is characterized by its index ($c^{index} = (c_{mix} - c_0) \times 100/c_0$), where the c_{mix} is the mixture concentration of the primary dendrites and the eutectic phase. Ghods et al. (2016a) proposed a simple equation to evaluate the mixture concentration (c_{mix}). Experimentally, c_{mix} is derived from the experimentally

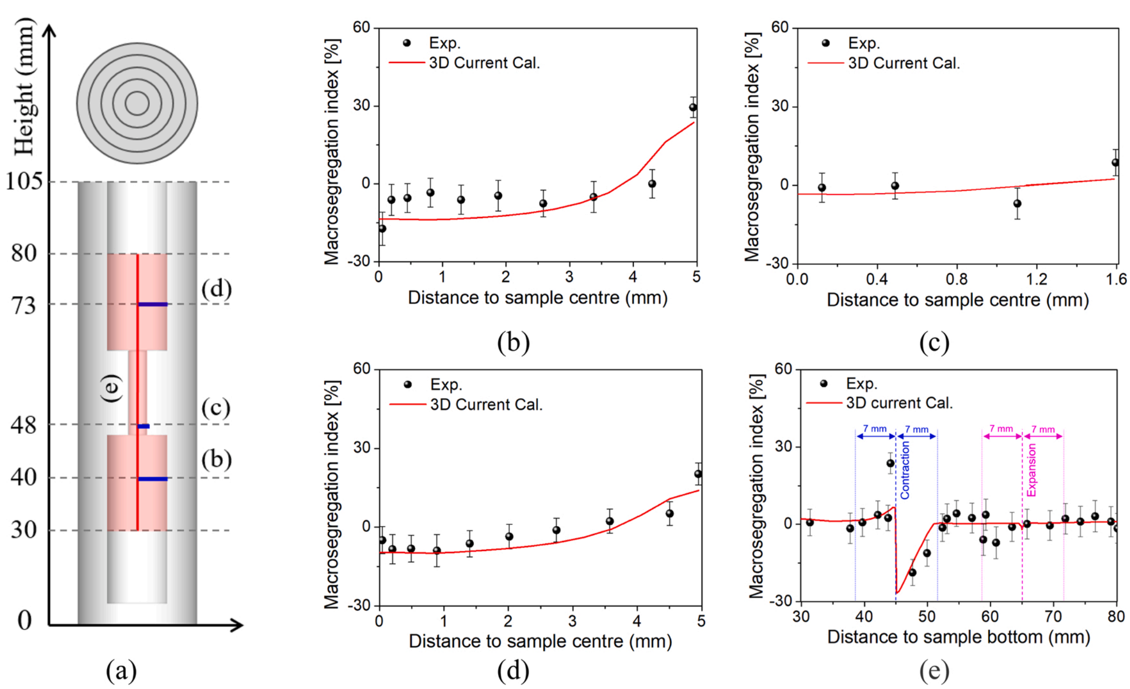

Fig. 5. Experiment–simulation comparison of the macrosegregation. (a) Schematic of the sample geometry and the evaluation method/positions for the macrosegregation measurement; (b)–(d) radial distribution of the macrosegregation (c^{index}) on different cross-sections, whose positions are marked in (a); (e) macrosegregation (section-averaged c^{index}) distribution along the axial direction. Black dots denote the experimental measurements, which are taken from Ghods et al. (2016b). The red lines denote the simulation results (For interpretation of the references to colour in this figure legend, the reader is referred to the web version of this article).

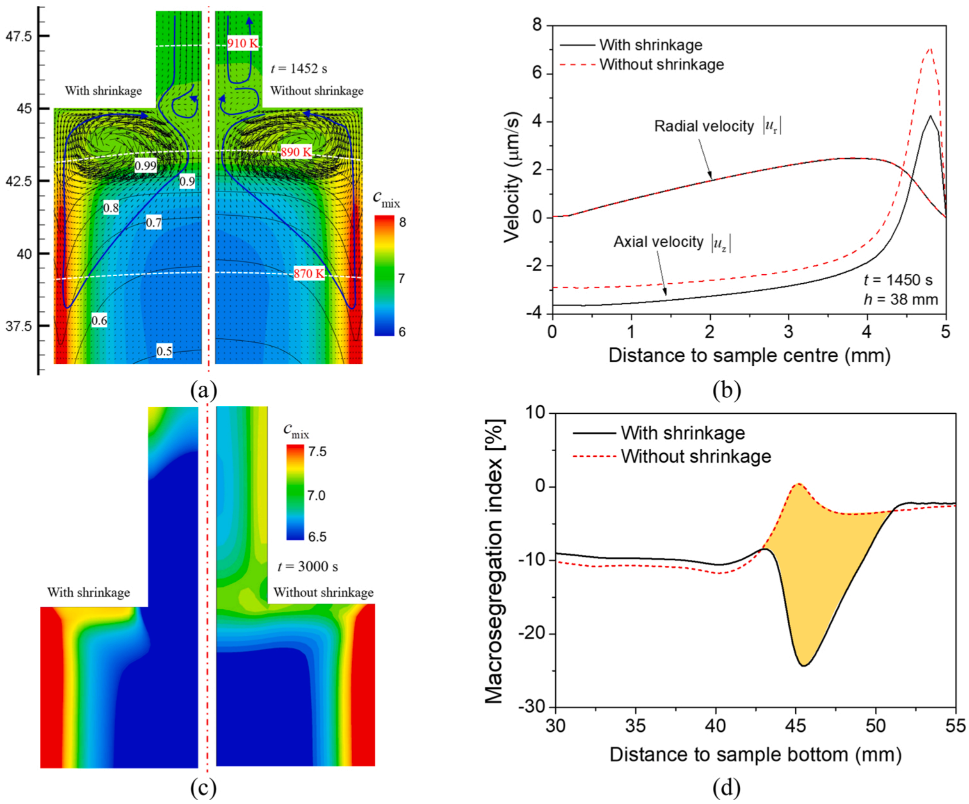

Fig. 6. Numerical analysis of the solidification shrinkage-induced feeding flow and its effect on the solidification by comparison of two simulation cases. Left-halves of (a) and (c) display the simulation case considering the solidification shrinkage in addition to the thermo-solutal convection; their right-halves display the simulation case ignoring shrinkage (pure thermo-solutal convection). (a) Contour of c_{mix} overlaid with isotherms (white dash lines), isopleths of the liquid volume fraction (dark solid lines), and vectors of the liquid velocity; the long blue vectors indicate the flow pattern; (b) comparison of the liquid velocity at the height of 38 mm; (c) c_{mix} contour at as-solidified state; (d) c_{mix} along the axis of the sample. These two cases were conducted with 2D axisymmetric model (For interpretation of the references to colour in this figure legend, the reader is referred to the web version of this article).

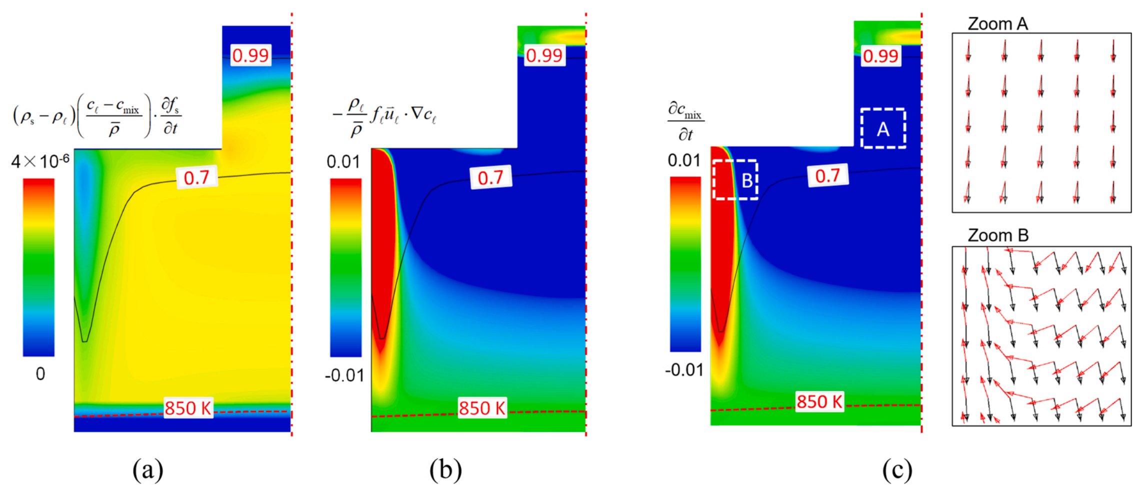

Fig. 7. Analyses of the macrosegregation mechanism for the moment at $t = 1580$s. (a) and (b) Contours of the first and second RHS terms in Eq. (1), overlaid by the isopleths of f_ℓ (back solid lines) and T_{eut} (red dash lines); (c) zoom-views of $\vec{u}_\ell$ (vectors in red) and ∇c_ℓ (vectors in black) (For interpretation of the references to colour in this figure legend, the reader is referred to the web version of this article).

determined volume fraction of the eutectic phase (f_{eut}) based on $c_{\mathrm{mix}} = (1.094 + 11.60 f_{\mathrm{eut}})/100$. To obtain the radial distribution of the macrosegregation, as schematically displayed in Fig. 5**(a)**, a series of concentric neighbouring rings was drawn on the transverse section of this sample. The volume fraction of eutectic phase (f_{eut}) in each ring was determined by measuring the area fraction of the eutectic phase using ImageJ, so that the average mixture concentration in this ring was calculated. Using the same method, the average c_{mix} over each transverse section was estimated by evaluating f_{eut} on the corresponding section. Fig. 5**(b)–(d)** display the radial macrosegregation distributions on different transverse sections, whose positions are marked in Fig. 5**(a)**. Excellent agreement between the experimental and the calculated results is obtained. Fig. 5**(e)** illustrates the axial macrosegregation (c^{index}) distribution. Both the experimental and calculated results exhibit a significant positive macrosegregation before the cross-section contraction, and then show strong negative macrosegregation after the cross-section contraction. Finally, the negative macrosegregation gradually recovers to a neutral composition along the axial direction. A weak negative macrosegregation, with the local minimum c^{index} of 3%, is numerically predicted at the position of the cross-section expansion; this minor negative macrosegregation appears difficult to detect experimentally. Note that the experimentally detected positive macrosegregation before the section contraction is underestimated by the simulation. The main reason is as follows. At that instant, when the

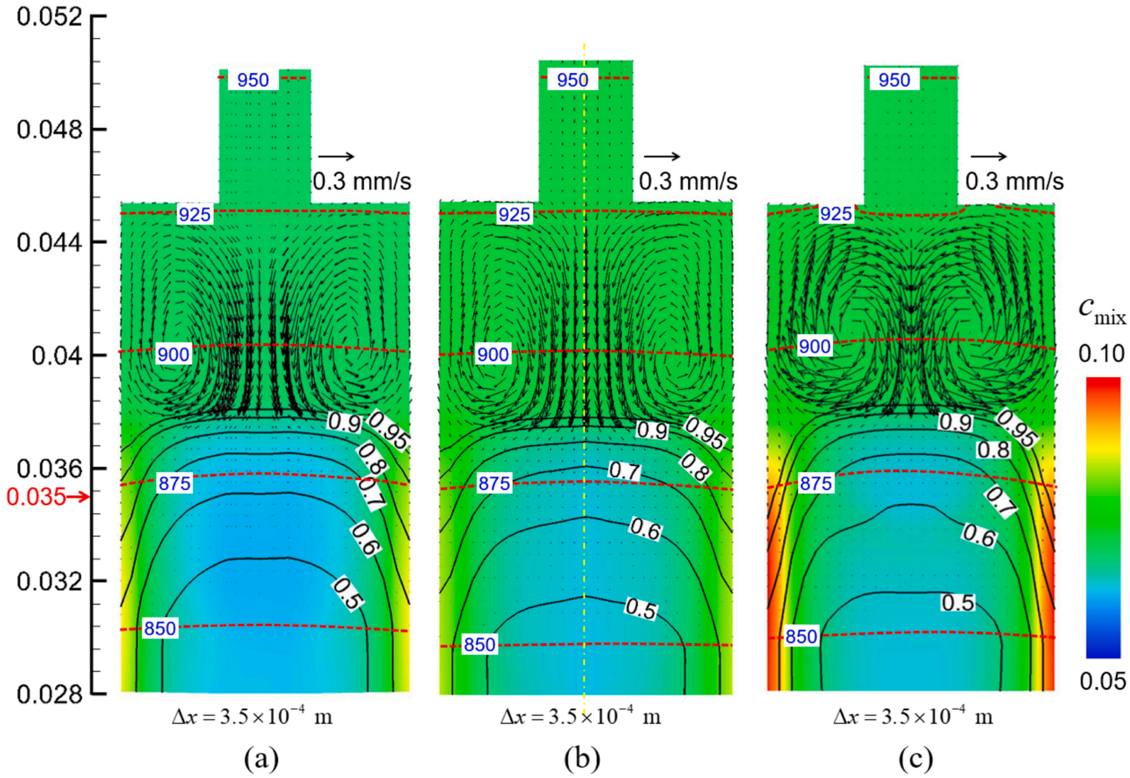

Fig. 8. Comparison of the simulations in 3D (a), 2D axi-symmetry (b) and 2D planar (c). The simulation results are evaluated at $t = 1272$s. Vectors denote the liquid velocity, colour scale represents c_{mix}, black solid lines are isopleths of f_ℓ, and red dash lines denote isotherms (For interpretation of the references to colour in this figure legend, the reader is referred to the web version of this article).

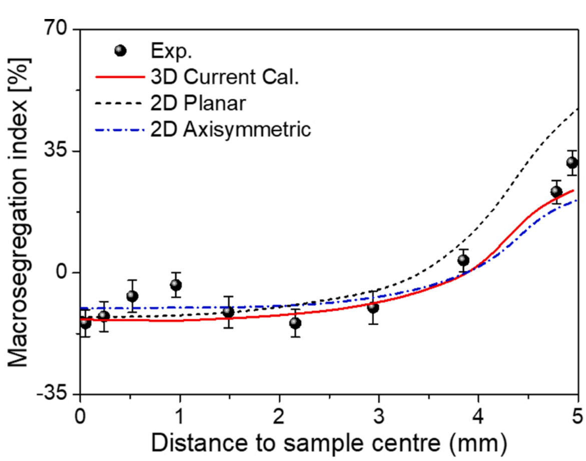

Fig. 9. Macrosegregation (c^{index}) profiles in as-solidified sample along the radial direction as calculated in different dimensions, in comparison with the experimental measurements.

mushy zone is passing the position of the cross-section contraction, referring to Fig. 2**(c)**, the as-solidified part of the sample shrinks and forms a gap between the sample and the mould, exactly below the shoulder; the interdendritic solute-enriched melt from the small section region is drained down and tends to feed the gap. This type of sample shrinkage and gap formation and the corresponding drainage and gap-feeding phenomena were ignored by the current model.

Note that the length of the sample used in the current simulation (100 mm) is shorter than the length of the sample in the experiments (300 mm). The reason is to reduce the calculation cost. The key feature of this sample is the cross-section change (contraction and expansion). In order to ensure the modelling accuracy, the length of the sample before and after the cross-section change must be larger than the thickness of a mushy zone. The mushy zone thickness is estimated as $(T_\ell - T_{\mathrm{eut}})/G$ i.e. ca. 7 mm. The length of the sample used in the current simulation (100 mm) is long enough to study the effect of the cross-section change on the solidification. In the first and third parts of the sample, where the diameter is ϕ9.5 mm, the length of the sample is 40 mm, ca. five times the thickness of the mushy zone. In the second part of the sample, where the diameter is ϕ3.2 mm, the length of the sample is equal to 20 mm, ca. three times of the thickness of the mushy zone. As shown in Fig. 5**(e)**, only near the cross-section contraction region, strong macrosegregation occurs. 7 mm away from the cross-section change, no evident macrosegregation is observed, i.e. macrosegregation index is nearly zero.

3.3. *Effect of shrinkage-induced feeding flow on macrosegregation*

To study the effect of the solidification-shrinkage-induced feeding flow on the solidification, an additional case is simulated by ignoring the solidification shrinkage, e.g. by assuming $\rho_\ell = \rho_s$ while keeping the thermo-solutal convection (Boussinesq approach). The simulation results of this case ($t = 1450$s), in comparison to the previous case considering both solidification shrinkage and thermo-solutal convection, are presented in Fig. 6**(a)**. Both the cases predict quite similar flow patterns and c_{mix} profiles in the large section zone. The isotherms and the isopleths of the liquid volume fraction are approximately the same. Main difference can be found in and near the small section zone. With the consideration of the shrinkage, a small vortex forms in the region of the section contraction. The melt from the small section flows downward besides the small vortex, to compensate the volume shrinkage in the mushy zone. Without the consideration of the shrinkage, a small vortex also forms there, but the melt in the small section is separated by this small vortex, so it cannot flow into the large section part.

The feeding flow is generally to compensate the solidification

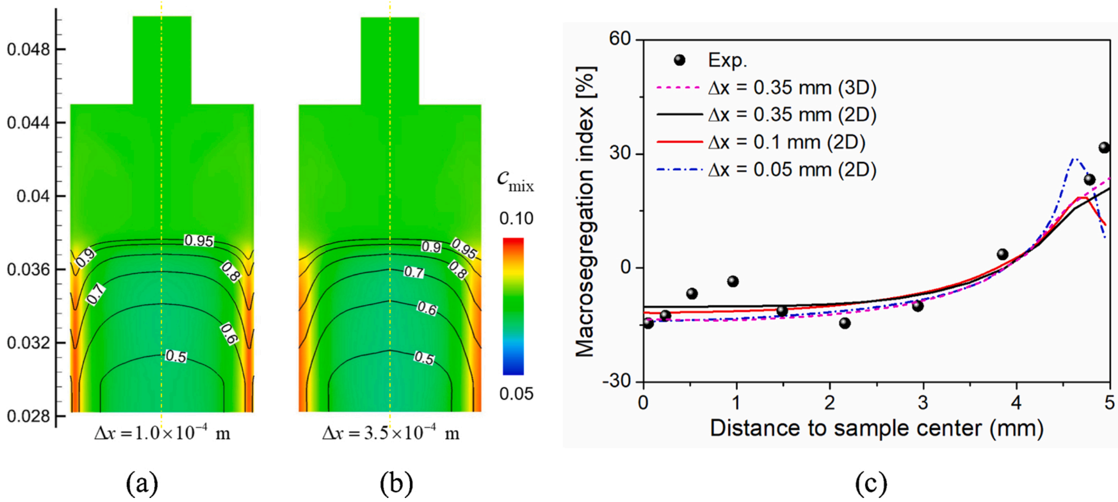

Fig. 10. Mesh sensitivity study. (a) and (b) contour of mixture concentration overlaid by the isolines of liquid phase fraction for cases with the fine mesh and the coarse mesh, respectively. (c) Macrosegregation profiles along the sample radius for different cases.

shrinkage. For this unidirectional solidification sample, the shrinkage-induced feeding flow is parallel to the melt convection in the sample centre, whereas near the sample surface, it is in the opposite direction to the melt convection. The liquid velocity components (u_r and u_z) are plotted in Fig. 6**(b)**. The shrinkage-induced feeding flow has almost no effect on the radial flow, but it strengthens the axial flow in the central part and suppresses the axial flow near the sample surface.

Fig. 6**(c)** depicts the as-solidified c_{mix} distribution. Significant difference is found in the lower part of the small section zone: the negative macrosegregation there for the case considering the shrinkage is not predicted by the case ignoring the shrinkage. This difference is more clearly seen in Fig. 6**(d)**, where the c_{mix} profiles along the sample axis are plotted. The orange area depicts the significant difference in the calculated c_{mix} of these two cases.

3.4. Mechanism of macrosegregation

Zhang et al. (2018) studied the feeding-flow-induced inverse segregation in the 1D solidification case. The simulation results were verified to be in line with the Flemings theory (Flemings et al., 1968). The following part is to analyse the feeding-flow-induced macrosegregation in multi-dimensions (2D or 3D) according to

$$\frac{\partial c_{\mathrm{mix}}}{\partial t} = (\rho_{\mathrm{s}} - \rho_{\ell})\left(\frac{c_{\ell} - c_{\mathrm{mix}}}{\overline{\rho}}\right)\cdot\frac{\partial f_{\mathrm{s}}}{\partial t} - \frac{\rho_{\ell}}{\overline{\rho}} f_{\ell}\vec{u}_{\ell}\cdot\nabla c_{\ell}. \tag{1}$$

The derivation of this equation can be found in **Appendix A**. Corresponding to the two right hand side (RHS) terms in Eq. (1), the local variation rate of c_{mix} is the outcome of two contributions. The first term is related to the solidification shrinkage, and the second term is due to the melt flow, where the flow can be caused by the solidification shrinkage, thermo-solutal convection, or geometry. An example of the macrosegregation mechanism analysis for the moment at 1580s is presented in Fig. 7. The first RHS term is always positive; the second RHS term can be negative/positive depending on the directions of the flow ($\vec{u}_{\ell}$) and the solute concentration gradient of the liquid phase (∇c_{ℓ}). The value of the second RHS term is several orders of magnitude larger than that of the first RHS term, indicating the dominant role of the second RHS term. Wu et al. (2008) found that if $f_{\ell}\vec{u}_{\ell}$ and ∇c_{ℓ} point in the similar direction (the angle less than 90°), the flow depletes the local c_{mix}. Specifically, the melt with a lower c_{ℓ} entering a region to replace the melt of a higher c_{ℓ} leads to depletion of c_{mix}. This mechanism operates in the small section zone (e.g. Zoom A of Fig. 7**(c)**). In the opposite situation (the angle larger than 90°), i.e. the melt with a higher c_{ℓ} entering a region to replace the melt of a lower c_{ℓ} leads to an increase in c_{mix}. This mechanism operates near the sample surface of the large section zone (e.g. Zoom B of Fig. 7**(c)**).

4. Discussion

Excellent quantitative simulation–experiment agreement is achieved regarding the macrosegregation in the unidirectionally solidified sample with a specially-designed geometry (cross-section contraction or expansion). In principle, each detail of the macrosegregation can be explained, e.g. by Eq. (1). From Fig. 7, the melt flow ($\vec{u}_{\ell}$) as part of the second RHS term of Eq. (1) plays the critical role in the formation macrosegregation, whereas from Figs. 2 and 3, $\vec{u}_{\ell}$ is largely dependent on the geometry. From this study, one can infer the importance of the geometry in some critical components, like turbine blades, which are cast with segregation-prone Ni-based superalloys. From computational fluid dynamics (CFD) perspective, all the flows are 3D in nature, and the numerical calculation accuracy depends on the mesh size. In this regard, some discussions are presented in the following sections.

4.1. 3D vs. 2D

Ghods et al. (2016a) have simulated the solidification process of this benchmark. Most experimentally observed phenomena were qualitatively explained. However, their simulations were based on a 2D planar model. In the current work, three simulations are conducted: full 3D, 2D axi-symmetry and 2D planar. They are compared in Figs. 8 and 9. The 2D axisymmetric calculation (Fig. 8**(b)**) can reproduce the 3D calculation well (Fig. 8**(a)**). The simulation results in 2D planar are displayed in Figs. 8**(c)** and 9. It can qualitatively reproduce the flow and the macrosegregation pattern, but the liquid velocity magnitude and the segregation severity are remarkably overestimated, particularly at the sample surface. Note that the above statement on the reproducibility of the full 3D calculation by the 2D axisymmetric calculation may be only applicable to the current casting sample possessing a small cross-section. For casting with large sections, the 3D nature of the flow may not be reproduced by a 2D asymmetrical model, even though the casting geometry is ideally asymmetrical.

4.2. Mesh sensitivity

Here only 2D axisymmetric calculations were conducted. The calculated macrosegregation in the as-cast sample using three mesh sizes

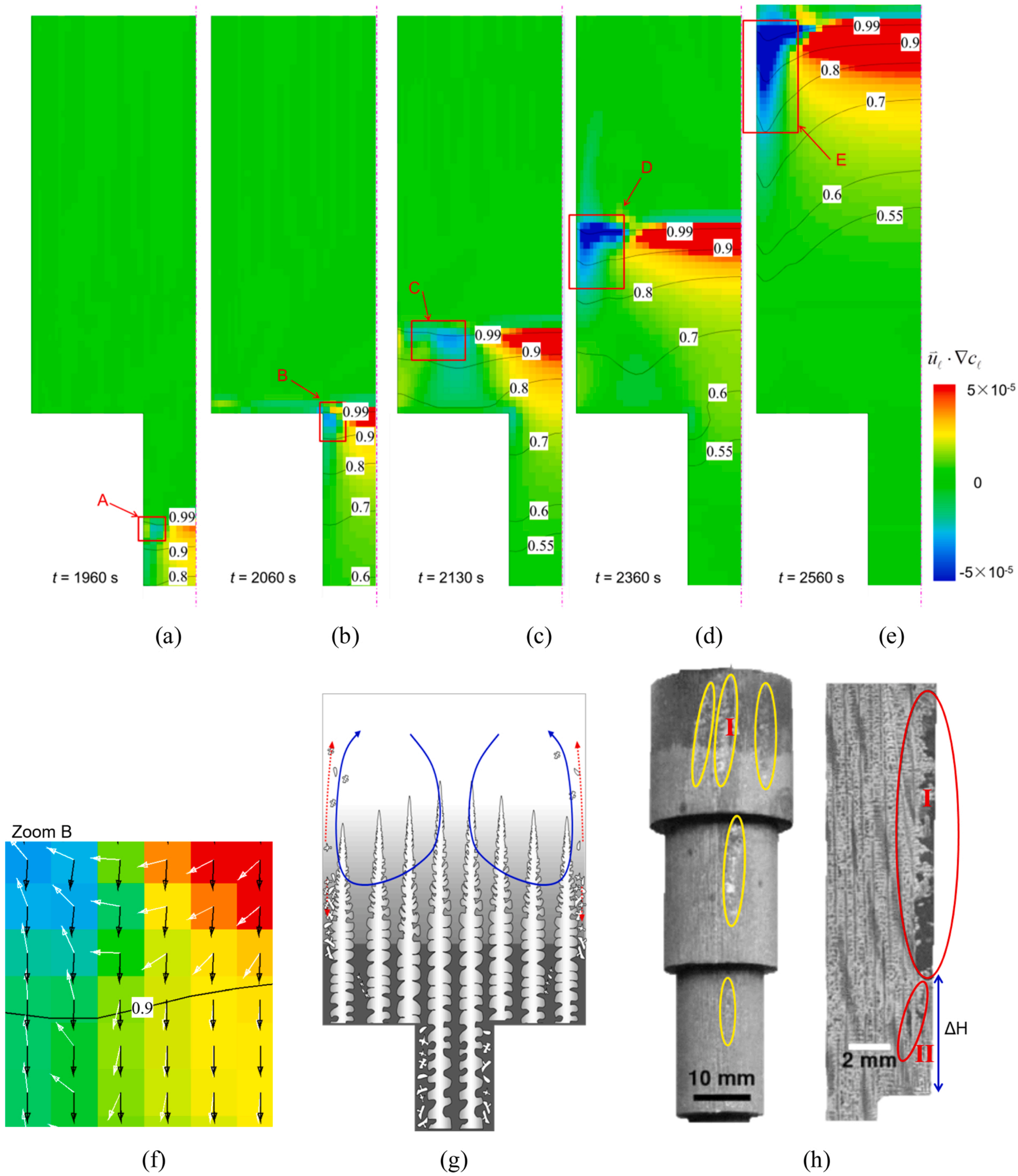

Fig. 11. Analysis of the possible formation of spurious/stray crystals. (a)–(e) Evolution sequence $\vec{u}_\ell \cdot \nabla c_\ell$ contours; (f) zoom-in view of Zoom B in (b); (g) schematics of the solidification and the melt flow; (h) Example of the stray crystals coupled with freckles in the laboratory castings. Figure (h) is cited from Ma et al. (2012), with permission of Springer Nature.

(0.35, 0.1, and 0.05 mm) are compared in Fig. 10. The contours of the mixture concentration (c_{mix}) for cases with the fine mesh and the coarse mesh are shown in Fig. 10**(a)** and **(b)**. They present similar segregation pattern. One minor difference between Fig. 10**(a)** and **(b)** is in the shape of the f_ℓ isopleth near the sample surface. The details of the f_ℓ distribution near the sample surface cannot be resolved appropriately by the course mesh (0.35 mm). Macrosegregation profiles along the sample radius for different cases with different mesh sizes are displayed in Fig. 10**(c)**. All the simulations display similar segregation profiles. The abrupt change in c^{index} due to the abrupt change in the f_ℓ distribution near the sample surface is not resolvable when the mesh is coarse (0.35 mm). This can also be seen in Figs. 8 and 9. When the simulation is conducted with a fine mesh smaller than 0.1 mm, the results can reproduce the experimental measurements well, except for one point at the sample surface. It can be concluded that the mesh size of 0.1 mm is sufficiently fine to predict all the details of the macrosegregation in this casting.

The experimental point on the casting surface, which is not correctly predicted by the simulation, may be owing to the ignorance of the shrinkage of the as-solidified dendrites in the mush by the model. It is known that the dendrite networks in the mushy zone shrink and form a tiny gap between the casting and the mould; thus, the interdendritic melt feeds the gap, intensifying the positive segregation on the sample surface. As discussed in Section 3.2.2 (Fig. 5**(e)**), in the macrosegregation profile along the axial direction, a relatively large simulation error occurs near the position of the sample section extraction. This is also due to the ignorance of the shrinkage of the as-solidified part of the sample. In that case, a gap between the casting and the mould exactly below the shoulder is formed and the interdendritic melt from the small section region is drained down and tends to feed the gap. This type of sample shrinkage and gap formation and the corresponding drainage and gap-feeding phenomena must be considered in the future models. It is well known that material properties are important factor for the accuracy of the simulation results. They are mostly temperature dependent. Due to limited data resource, here they are treated as constant. The satisfied simulation-experiment agreement regarding to the macrosegregation distribution along the casting sample (Fig. 5) seems to verify that this simplification is acceptable for the case of the current laboratory experiment conditions. However, it is highly recommended more precise temperature-dependent properties should be used when this model is applied for simulation of engineering castings.

4.3. Possible formation of spurious crystals

As reported by Ma and Bührig-Polaczek (2014), spurious/stray crystals are serious casting defects during the production of turbine blades. They appear frequently along with the formation of freckles. Hellawell et al. (1997) believed that re-melting of the secondary or high-order dendrites, as enhanced by the interdendritic melt flow, is the main formation mechanism of the dendrite fragmentation, which serves as the origin of spurious/stray crystals. The detachment of fragments from the dendrite tip region of Al-10 wt.% Cu alloy was experimentally observed by Zimmermann et al. (2017). Zheng et al. (2018) have previously suggested a simple formulation in a three-phase solidification model for the crystal fragmentation: $M_{\rm ce} = -\gamma \cdot \rho_\ell \cdot \vec{u}_\ell \cdot \nabla c_\ell$, where $M_{\rm ce}$ is the mass transfer rate from the columnar to equiaxed phases, attributed to the production of fragments (spurious crystals). This suggests that the interdendritic flow ($\vec{u}_\ell$) in the direction opposite to the melt concentration gradient ($-\nabla c_\ell$) in the mush will promote fragmentation. However, this formulation cannot be used here to predict the formation of spurious crystals, because the so-called fragmentation coefficient, γ, is unknown and should be determined experimentally. Interestingly, the formation of spurious crystals appears to be strongly related to $\vec{u}_\ell \cdot \nabla c_\ell$, i.e. the same driving force for the onset of freckles (flow-induced macrosegregation). Therefore, $\vec{u}_\ell \cdot \nabla c_\ell$ is used here to analyse the possible formation of spurious crystals.

Fig. 11**(a)**–**(e)** display the evolution sequence of $\vec{u}_\ell \cdot \nabla c_\ell$. A zoom-in view of Zoom B, as marked by the red rectangle in Fig. 11**(b)**, is presented in Fig. 11**(f)**. In the 'blue' region with a negative value of $\vec{u}_\ell \cdot \nabla c_\ell$, where the angle between vectors $\vec{u}_\ell$ and ∇c_ℓ is larger than 90°, spurious crystals are prone to form. This blue region is mostly located close to the casting surface and near the front of mushy zone, where flow is still quite strong. With time evolution (from 1960 to 2560s), when the solidification front advances from the small cross-section to the large cross-section regions, the magnitude of $|\vec{u}_\ell \cdot \nabla c_\ell|$ increases, i.e. the probability to form spurious crystals increases. To assist in understanding the mechanism, the melt flow and the solidification are depicted in Fig. 11 **(g)** schematically. The spurious crystals, attributed to the solute-driven re-melting of dendrites, possibly form near the sample surface. Few of them may be transported by the flow into the bulk liquid region and re-melted completely; however, most of them might be captured by the columnar dendrites and develop into freckle chains there.

Although no remarkable spurious crystals were observed on the sample of Al–7.0 wt.% Si alloy in Gohds' experiments (Ghods et al., 2018), several small misoriented dendrite fragments were detected. Ma et al. (2012) conducted a series of unidirectional solidification experiments with similar casting geometry (cross-section changes) on superalloys, and more evidences were found. Specifically, the formation of spurious/stray crystals and freckle chain was correlated to the abrupt cross-section expansion, as displayed in Fig.11**(h)**. As reported by Ma et al. (2012), at the position of the abrupt section expansion, the freckle chain in the small cross-section zone cannot extend immediately along the bottom edge of the large cross-section zone, but it continues to appear after an incubation height of about $\Delta H = 10$. From the longitudinal section of the casting sample, it can be seen that below the position of the surface freckle chain (freckle I), a short but clear under-surface freckle (freckle II) forms. Although we did not perform the numerical simulations of the experiments as conducted by Ma et al. (2012), the current modelling results (Fig. 11**(a)–(f)**) provide relevant information to explain the experimental observations. Immediately after the solidification front passes the position of the cross-section expansion (Figs. 3 **(a)** and 11**(b)**), the flow is so weak that spurious crystals may not form. In the next moment, Figs. 3**(b)** and 11**(c)**, the flow becomes stronger but is still not sufficiently strong to form freckle and spurious crystals at the sample surface; some under-surface freckle (freckle II) may form. Only when the flow is sufficiently strong (Figs. 3**(c)** and 11**(d)** and **(e)**), surface freckles (freckle I) can generate.

5. Conclusions

In this study, a two-phase solidification model is employed to simulate the solidification benchmark with cross-section changes (Ghods et al., 2016a). Along the solidification direction, the diameter of the sample changes between ϕ9.5 and ϕ3.2 mm, highlighting the geometrical effect on the solidification. Excellent agreement is obtained between the experiment and the simulation regarding macrosegregation and phase distribution in the as-solidified sample. The numerical model is verified.

The main effect of the geometry on the unidirectional solidification is the modification of the bulk and the interdendritic flow during solidification, leading to the formation of macrosegregation and spurious/stray crystals in several critical locations.

- The flow originates from the solidification shrinkage and the thermo-solutal convection. Without any cross-sectional change, the thermo-solutal buoyancy dominates the flow, and a so-called 'steepling convection' is induced, leading to a relatively strong positive macrosegregation near the sample surface.
- With the cross-section contraction, the space for the flow is largely limited by the sample geometry, and a severe positive macrosegregation under the 'shoulder' of the cross-section contraction is induced.
- The solidification-shrinkage-induced feeding flow is magnified in the small cross-section part, where a negative segregation is formed.
- The cross-section expansion in the geometry leads to a high risk for the formation of spurious/stray crystals.

A mathematical equation (Eq. (1)) is derived to analyse the macrosegregation. The scalar product of the flow velocity and the concentration gradient of the melt ($\vec{u}_\ell \cdot \nabla c_\ell$) can be used to analyse the formation of macrosegregation and spurious/stray crystals.

- Positive and negative segregation occur at the locations where the negative and positive values of $\vec{u}_\ell \cdot \nabla c_\ell$ are distributed, respectively.
- Freckles and spurious crystals are formed at the locations where the negative value of $\vec{u}_\ell \cdot \nabla c_\ell$ is distributed.

The numerical simulation accuracy regarding the mesh quality is validated. Full 3D, 2D axi-symmetry, and 2D planar simulations are compared. For the current cylindrical sample having a small diameter, the 2D axi-symmetry simulation can reproduce the result of the full 3D calculation.

CRediT authorship contribution statement

Haijie Zhang: Conceptualization, Methodology, Investigation, Writing - original draft, Visualization. **Menghuai Wu:** Conceptualization, Methodology, Writing - review & editing, Project administration. **Surendra N. Tewari:** Conceptualization, Validation, Writing - review & editing. **Andreas Ludwig:** Conceptualization, Supervision. **Abdellah Kharicha:** Conceptualization, Software.

Declaration of Competing Interest

None.

Acknowledgements

This work was supported by FFG – ASAP (No. 859777), FWF (I 4278 - N36), and ESA - MICAST. Support from NASA grant NNX14AM18G is gratefully acknowledged.

Appendix A. Solidification-shrinkage-induced macrosegregation

The mixture density, ($\overline{\rho}$),

$$\overline{\rho} = f_\ell \rho_\ell + f_s \rho_s. \tag{A.1}$$

The mass conservation equations are

$$\frac{\partial (f_s \rho_s)}{\partial t} + \nabla\cdot(f_s \rho_s \vec{u}_s) = M_{\ell s}, \tag{A.2}$$

$$\frac{\partial (f_\ell \rho_\ell)}{\partial t} + \nabla\cdot(f_\ell \rho_\ell \vec{u}_\ell) = -M_{\ell s}, \tag{A.3}$$

where $M_{\ell s}$ indicates the mass transfer rate from the liquid to the solid.

The sum of Eq. (A.2) and Eq. (A.3) yields

$$\frac{\partial \overline{\rho}}{\partial t} = -\nabla\cdot\left(f_\ell \rho_\ell \vec{u}_\ell\right) \tag{A.4}$$

The species conservation equations are

$$\frac{\partial (f_s \rho_s c_s)}{\partial t} + \nabla\cdot(f_s \rho_s c_s \vec{u}_s) = \nabla\cdot(f_s \rho_s D_s \nabla c_s) + C_{\ell s}, \tag{A.5}$$

$$\frac{\partial (f_\ell \rho_\ell c_\ell)}{\partial t} + \nabla\cdot(f_\ell \rho_\ell c_\ell \vec{u}_\ell) = \nabla\cdot(f_\ell \rho_\ell D_\ell \nabla c_\ell) - C_{\ell s}, \tag{A.6}$$

where $C_{\ell s}$ is the species exchange between the solid and the liquid.

By ignoring the solute diffusion at the macroscopic scale ($D_\ell = D_s = 0$), the sum of Eq. (A.5) and (A.6) yields

$$\overline{\rho}\frac{\partial c_{\mathrm{mix}}}{\partial t} + c_{\mathrm{mix}}\frac{\partial \overline{\rho}}{\partial t} + c_\ell \nabla\cdot(f_\ell \rho_\ell \vec{u}_\ell) + f_\ell \rho_\ell \vec{u}_\ell\cdot\nabla c_\ell = 0. \tag{A.7}$$

Substituting Eq. (A.4) into (A.7), the varying rate of the mixture concentration is obtained as follows:

$$\frac{\partial c_{\mathrm{mix}}}{\partial t} = (\rho_s - \rho_\ell)\left(\frac{c_\ell - c_{\mathrm{mix}}}{\overline{\rho}}\right)\cdot\frac{\partial f_s}{\partial t} - \frac{\rho_\ell}{\overline{\rho}} f_\ell \vec{u}_\ell\cdot\nabla c_\ell. \tag{A.8}$$

References

Flemings, M.C., Mehrabian, R., Nereo, G.E., 1968. Macrosegregation: part II. Trans. Metall. Soc. AIME 241, 41–49.

Ghods, M., Johnson, L., Lauer, M., Grugel, R.N., Tewari, S.N., Poirier, D.R., 2016a. Radial macrosegregation and dendrite clustering in directionally solidified Al-7Si and Al-19Cu alloys. J. Cryst. Growth 441, 107–116. https://doi.org/10.1016/j.jcrysgro.2016.02.014.

Ghods, M., Johnson, L., Lauer, M., Grugel, R.N., Tewari, S.N., Poirier, D.R., 2016b. Macrosegregation in Al-7Si alloy caused by abrupt cross-section change during directional solidification. J. Cryst. Growth 449, 134–147. https://doi.org/10.1016/j.jcrysgro.2016.06.010.

Ghods, M., Lauer, M., Upadhyay, S.R., Grugel, R.N., Tewari, S.N., Poirier, D.R., 2018. Spurious grain formation at cross-sectional expansion during directional solidification: influence of thermosolutal convection. J. Mater. Eng. Perform. 27, 3122–3130. https://doi.org/10.1007/s11665-018-3364-0.

Hellawell, A., Liu, S., Lu, S.Z., 1997. Dendrite fragmentation and the effects of fluid flow in castings. JOM 49, 18–20. https://doi.org/10.1007/BF02914650.

Hong, J., Ma, D., Wang, J., Wang, F., Dong, A., Sun, B., Bührig-Polaczek, A., 2015. Geometrical effect of freckle formation on directionally solidified superalloy CM247 LC components. J. Alloys. Compd. 648, 1076–1082. https://doi.org/10.1016/j.jallcom.2015.07.016.

Lipton, J., Glicksman, M.E., Kurz, W., 1984. Dendritic growth into undercooled alloy metals. Mater. Sci. Eng. 65, 57–63. https://doi.org/10.1016/0025-5416(84)90199-X.

Ma, D., Bührig-Polaczek, A., 2014. The geometrical effect on freckle formation in the directionally solidified superalloy CMSX-4. Metall. Mater. Trans. A Phys. Metall. Mater. Sci. 45, 1435–1444. https://doi.org/10.1007/s11661-013-2088-x.

Ma, D., Wu, Q., Bührig-Polaczek, A., 2012. Some new observations on freckle formation in directionally solidified superalloy components. Metall. Mater. Trans. B Process Metall. Mater. Process. Sci. 43, 344–353. https://doi.org/10.1007/s11663-011-9608-0.

Magnusson, T., Arnberg, L., 2001. Density and solidification shrinkage of hypoeutectic aluminum-silicon alloys. Metall. Mater. Trans. A Phys. Metall. Mater. Sci. 32, 2605–2613. https://doi.org/10.1007/s11661-001-0050-9.

Wu, M., Könözsy, L., Ludwig, A., Schützenhöfer, W., Tanzer, R., 2008. On the formation of macrosegregations in steel ingot castings. Steel Res. Int. 79, 637–644. https://doi.org/10.1002/srin.200806177.

Wu, M., Zheng, Y., Kharicha, A., Ludwig, A., 2016. Numerical analysis of macrosegregation in vertically solidified Pb-Sn test castings – part I: columnar solidification. Comput. Mater. Sci. 124, 444–455. https://doi.org/10.1016/j.commatsci.2016.07.017.

Wu, M., Ludwig, A., Kharicha, A., 2019. Volume-averaged modeling of multiphase flow phenomena during alloy solidification. Metals (Basel) 9, 229. https://doi.org/10.3390/met9020229.

Zhang, H., Wu, M., Zheng, Y., Ludwig, A., Kharicha, A., 2018. Macrosegregation formation in an Al–Si casting sample with cross-sectional change during directional solidification. Trans. Indian Inst. Met. 71, 2639–2643. https://doi.org/10.1007/s12666-018-1422-9.

Zhang, H., Wu, M., Zheng, Y., Ludwig, A., Kharicha, A., 2020. Numerical study of the role of mush permeability in the solidifying mushy zone under forced convection. Mater. Today Commun. 22, 100842. https://doi.org/10.1016/j.mtcomm.2019.100842.

Zheng, Y., Wu, M., Kharicha, A., Ludwig, A., 2018. Incorporation of fragmentation into a volume average solidification model. Model. Simul. Mater. Sci. Eng. 26, 015004. https://doi.org/10.1088/1361-651X/aa86c5.

Zimmermann, G., Pickmann, C., Hamacher, M., Schaberger-Zimmermann, E., Neumann-Heyme, H., Eckert, K., Eckert, S., 2017. Fragmentation-driven grain refinement in directional solidification of AlCu10wt-% alloy at low pulling speeds. Acta Mater. 126, 236–250. https://doi.org/10.1016/j.actamat.2016.12.063.